Journal of Power Sources 270 (2014) 158–165

Contents lists available at ScienceDirect

Journal of Power Sources

journal homepage: www.elsevier.com/locate/jpowsour

Recycling of cobalt from spent Li-ion batteries as β-$Co(OH)_2$ and the application of Co_3O_4 as a pseudocapacitor

E.M.S. Barbieri, E.P.C. Lima, M.F.F. Lelis, M.B.J.G. Freitas*

Federal University of Espírito Santo, Chemistry Department, Laboratory of Electrochemistry and Electroanalytics, Av. Fernando Ferrari, 514, Goiabeiras, Vitória, ES 29075-910, Brazil

HIGHLIGHTS

- Recycling cobalt from spent Li-ion batteries as $Co(OH)_2$ and Co_3O_4.
- Morphological and structural characterization of recycled $Co(OH)_2$ and Co_3O_4.
- Electrochemical characterization of Co_3O_4 composite electrodes.
- Co_3O_4 composites as promising pseudocapacitors.

ARTICLE INFO

Article history:
Received 10 April 2014
Received in revised form
8 July 2014
Accepted 16 July 2014
Available online 24 July 2014

Keywords:
Recycling
Li-ion batteries
Cobalt hydroxide
Cobalt oxide
Pseudocapacitor

ABSTRACT

This work has investigated recycling cobalt from the cathodes of spent Li-ion batteries as β-$Co(OH)_2$, obtaining Co_3O_4. β-$Co(OH)_2$ with a hexagonal structure by using chemical precipitation (CP) or electrochemical precipitation (EP). In addition, the study has investigated whether the charge density applied directly affects the β-$Co(OH)_2$ morphology. Co_3O_4 is formed by heat-treating β-$Co(OH)_2$ at 450 °C for 3 h (h) in an air atmosphere. After calcining, the Co_3O_4 shows a cubic structure and satisfactory purity grade, regardless of the route used for preparation via which it was obtained. Cyclic voltammetry (CV) is then used for electrochemical characterization of the Co_3O_4 composite electrodes. In the cathodic process, CoO_2 undergoes reduction to CoOOH, which undergoes further reduction to Co_3O_4. In the anodic process, Co_3O_4 undergoes oxidation to CoOOH, which simultaneously undergoes further oxidation to CoO_2. The composite electrodes containing Co_3O_4, carbon black, and epoxy resin show great reversibility, charge efficiency, and a specific capacitance of 13.0 F g^{-1} (1.0 mV s^{-1}). The synthesis method of $Co(OH)_2$ influences the charge efficiency of Co_3O_4 composite electrodes at a scan rate of 10.0 mV s^{-1}. Therefore, in addition to presenting an alternative use for exhausted batteries, Co_3O_4 composites exhibit favorable characteristics for use as pseudocapacitors.

1. Introduction

Lithium-ion (Li-ion) batteries, introduced to the consumer market by Sony in 1990, have gained prominence due to their desirable physicochemical characteristics, such as high energy density, a low rate of self-discharge, long life cycle, and high potential [1,2].The electrolyte in Li-ion batteries is an inorganic salt of lithium (Li) that is dissolved in a solvent or a mixture of organic solvents. $LiCoO_2$, which has a lamellar structure, is the most widely used cathode material. Graphite is used in the anode, forming the compound LiC_x ($0 < x < 6$) in the charge process [3].The charge and discharge processes of Li-ion batteries with $LiCoO_2$ cathodes are represented by the following equation.

$$LiCoO_2 + C_6 \underset{\text{Discharge process}}{\overset{\text{Charge process}}{\rightleftharpoons}} Li_{(1-x)}CoO_2 + Li_xC_6 \qquad (1)$$

The large increase in production and consumption of batteries has had serious effects, both environmentally and economically. To mitigate these effects, an alternative to discarding exhausted devices is to recycle them. This method is beneficial due to the large amount of cobalt present in spent Li-ion batteries [4]. For example, according to the London Metal Exchange (LME), in February of 2014, the price of cobalt was $31.20 kg^{-1} [5].

In general, crystalline cobalt oxides occur in distinct phases: CoO, Co_2O_3, and Co_3O_4. The Co_3O_4 crystalline phase is useful for

* Corresponding author. Tel.: +55 27 40097823; fax: +55 27 40092826.
E-mail addresses: marcosbj@hotmail.com, marcosbjg@gmail.com (M.B.J.G. Freitas).

http://dx.doi.org/10.1016/j.jpowsour.2014.07.108
0378-7753/

many applications because of its thermodynamic stability and desirable electrochemical properties [6]. This phase is thermodynamically stable because it is not reactive in the environment, and it retains its chemical and structure on the timescale of its expected usefulness. In particular, usefulness is retained in the presence of the alkaline solution and heat and during the charge and discharge cycles. The electrochemical properties of Co_3O_4 in the charge and discharge cycles are great reversibility, reproducibility, and cycle life. Co_3O_4, recently featured as a promising material for use in anodes for Li-ion batteries [7–9], also shows favorable characteristics for use in pseudocapacitors [10–12], chemical sensors [13], catalysts [14], thermal solar energy collectors [14], and electrochromic devices [6,15,16].

Therefore, scientific research has been directed not only toward developing processes of recovering and recycling cobalt from spent Li-ion batteries, but also toward developing more efficient materials for energy conversion, electrocatalysis, and electrochromic systems. In this work, cobalt from the cathodes of spent Li-ion batteries was recycled as $Co(OH)_2$, using chemical or electrochemical precipitation. Co_3O_4 then was synthesized via thermal treatment of the $Co(OH)_2$. Finally, the electrochemical properties of composite electrodes containing Co_3O_4, carbon black, and epoxy resins as a binder were analyzed using cyclic voltammetry (CV). Techniques used for material characterization included X-ray diffractometry (XRD), Raman scattering spectroscopy, Fourier transform infrared (FT-IR), and scanning electronic microscopy (SEM).

2. Experimental

2.1. Dissolution of the cathodes of spent Li-ion batteries

The cathode of a Samsung® 3.7 V BST Li-ion battery was separated and dried at 120 °C for 24 h (h), after which it was washed with deionized water at 40 °C and dried at 60 °C for another 24 h. Next, active material was separated from the aluminum substrate. A mass of 10.0 g of active material was dissolved in 1.0 L of a solution of 3.0 mol L^{-1} HNO_3 by stirring for 2 h at 80 °C. The solution of the cathode dissolution was filtered, removing insoluble materials such as graphite. This dissolution process may be represented by the following chemical equation.

$$4LiCoO_{2(s)} + 12HNO_{3(aq)} \rightarrow 4LiNO_{3(aq)} + 4Co(NO_3)_{2(aq)} + 6H_2O_{(l)} + O_{2(g)} \quad (2)$$

2.2. Chemical and electrochemical precipitation of $Co(OH)_2$ precursor material

The solution of cathode dissolution made from spent Li-ion batteries was used for chemical and electrochemical precipitation of the precursor material, $Co(OH)_2$. In chemical precipitation (CP), $Co(OH)_2$ was obtained by adding 1.0 mol L^{-1} KOH to the Co^{2+} solution. The rate of addition of the 1.0 mol L^{-1} KOH solution was 0.034 mL sec^{-1}. The pH was recorded after each 1.0 mL of 1.0 mol L^{-1} KOH solution was added to the Co^{2+} solution, and it was found that the pH at which $Co(OH)_2$ precipitation occurred was 7.5–8.0 [17,18]. In electrochemical precipitation (EP), the pH of the cathode dissolution was 6.5 with the addition of KOH pellets and buffering with H_3BO_3 at a concentration of 0.1 mol L^{-1}. EP of $Co(OH)_2$ films was performed in a cell with three electrodes: aluminum (Merck 99.99% w/w) with an area of 0.5 cm^2 was used as a working electrode, graphite (3.7 cm^2 area) was used as a counter electrode, and Ag/AgCl (NaCl 3.0 mol L^{-1}) was used as a reference electrode. CV started from an open-circuit potential of −0.56 V and progressed to a cathode potential of −1.5 V. In the reverse scan, a maximum potential of 0.0 V was seen, and this returned to −0.56 V at scan rates of 1.0 mV s^{-1}, 5.0 mV s^{-1}, and 10.0 mV s^{-1}. The growth of $Co(OH)_2$ films was studied by varying the charge density as follows: 0.5 C cm^{-2}, 1.0 C cm^{-2}, 1.5 C cm^{-2}, 2.0 C cm^{-2}, 2.5 C cm^{-2}, 3.0 C cm^{-2}, 5.0 C cm^{-2}, 7.0 C cm^{-2}, and 10.0 C cm^{-2}. $Co(OH)_2$ films were scraped from the electrodes after the potentiostatic formation process.

Table 1
Composite electrode composition.

Composite	Co_3O_4 (mg)	Carbon black (mg)	Epoxy resin (mg)
$CP80_{CB}$	17.7	3.3	1.1
$EP80_{CB}$	17.5	3.2	1.0

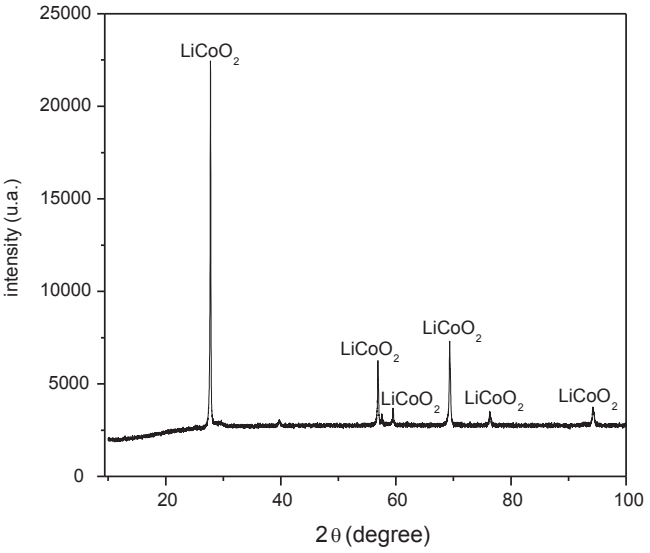

Fig. 1. Typical x-ray diffraction spectrum of a positive electrode from a spent Li-ion battery.

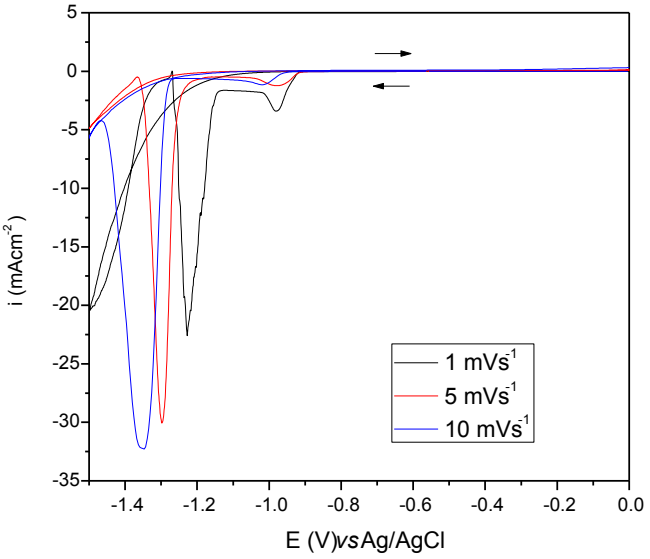

Fig. 2. Typical cyclic voltammograms performed at scan rates of 1.0 mV s^{-1}, 5.0 mV s^{-1}, and 10.0 mV s^{-1} for CP and EP electrodes.

2.3. Preparation and electrochemical analysis of the Co_3O_4-carbon black-epoxy resin composite electrodes

$Co(OH)_2$ obtained via CP or EP (10.0 C cm^{-2}) was calcined at 450 °C for 3 h in an air atmosphere for synthesis of the Co_3O_4-carbon black-epoxy resin composite electrodes [6,9–16,19]. The substrate used to prepare the working electrode was a grid of Ni–Fe with a geometric area of 0.7 cm^2 extracted from Ni-MH batteries, copper wire as an electrical contact, and epoxy resin as the insulating material.

Table 1 shows characteristics of the composite electrodes of Co_3O_4. Chloroform, in 2 mL measures, was added to the mixture of Co_3O_4-carbon black-epoxy resin to homogenize the paste. After 10 min homogenization, 1.0 mL paste was placed on the substrate. The electrode was left at room temperature for 24 h to allow for evaporation of the chloroform and curing of the resin [20]. Composite electrodes then were analyzed using CV with an initial potential of 0.2 V, a maximum potential of 0.5 V, and scan rates of 1.0 mV s^{-1} and 10 mV s^{-1}. The 6.0 mol L^{-1} KOH solution was used as an electrolyte, and Hg/HgO and graphite with an area of 3.0 cm^2 were used as the reference electrode and counter electrode, respectively. All electrochemical measurements were performed without stirring, at 25 °C.

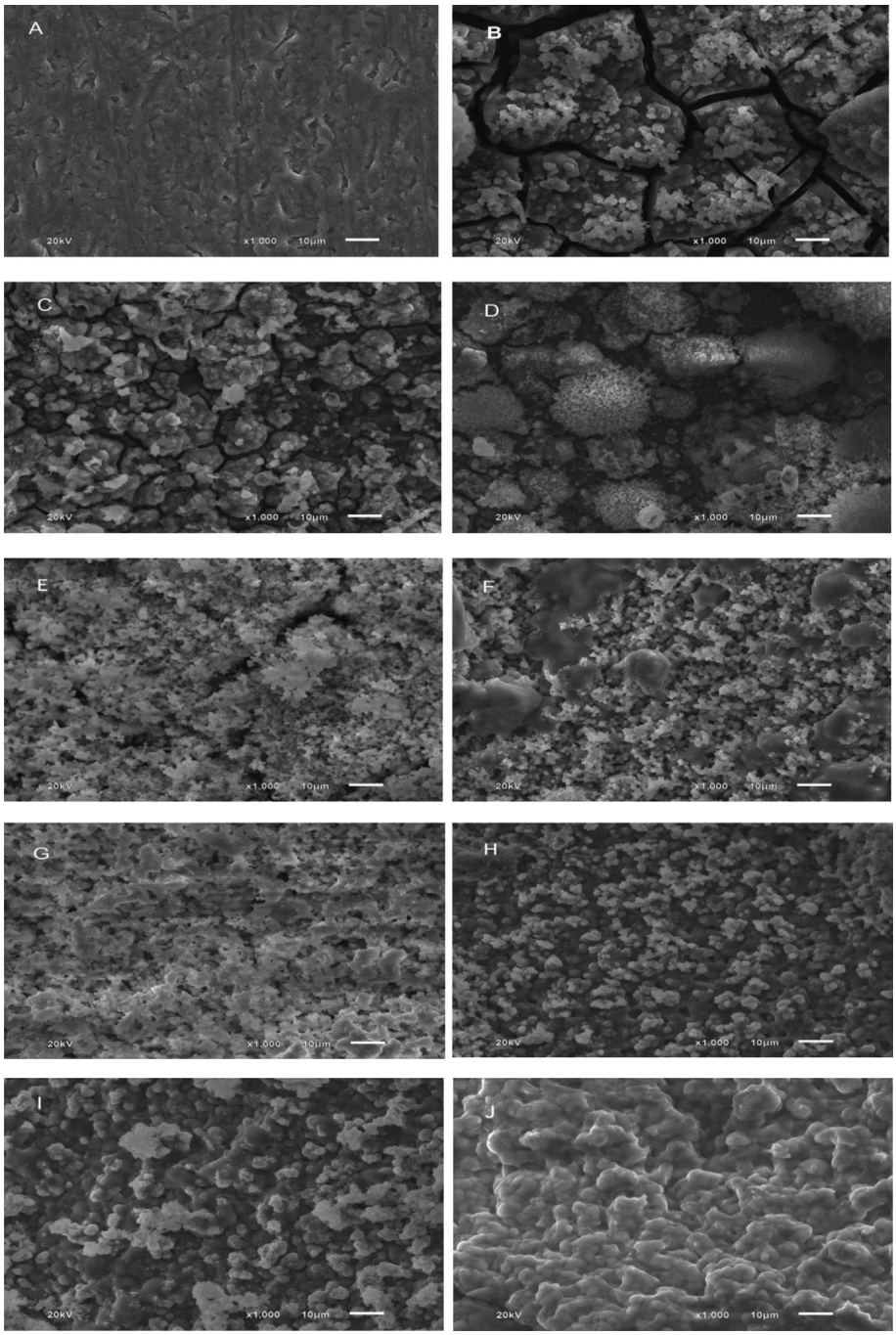

Fig. 3. Micrographs of the $Co(OH)_2$ recovered by electrochemical precipitation:(A) Al, (B) 0.5 C cm^{-2}, (C) 1.0 C cm^{-2}, (D) 1.5 C cm^{-2}, (E) 2.0 C cm^{-2}, (F) 2.5 C cm^{-2}, (G) 3.0 C cm^{-2}, (H) 5.0 C cm^{-2}, (I) 7.0 C cm^{-2}, and (J) 10.0 C cm^{-2}.

2.4. Equipment used for materials characterization

All electrochemical measurements were performed using Autolab PGSTAT 302N potentiostat/galvanostat equipment with an electrochemical impedance spectroscopy module (EIS).

Diffraction measurements were carried out using Shimadzu XRD-600 equipment, model 20013, with CuKα ($\lambda = 1.5418$ Å) radiation and Bruker equipment, model D2 Phaser, with CuKα ($\lambda = 1.5406$ Å) radiation and a scan rate of 2 per min.

Micrographs were carried out using a JEOL 6610LV scanning electron microscope. Composition of $Co(OH)_2$ was determined via Raman spectroscopy, specifically, module AFM Alpha 300 WITEC. Absorption spectra in the infrared region were obtained using the Fourier Transform Infrared (FT-IR) 400 Spectrometer from Perkin Elmer, using ATR with a resolution of 4 cm^{-1} and 32 scans. Thermal analyses were performed in an air atmosphere. For this, the SDT Q600 V20.9 Build 20 module DSC-TGA Standard was used, with an air flow of 100 mL min^{-1}, a heating rate of 20 °C min^{-1}, and a maximum temperature of 900 °C.

3. Results and discussion

3.1. Characterization of cathode material from spent Li-ion batteries

Fig. 1 shows a typical diffractogram of cathode material from spent Li-ion batteries. A comparison of peaks in the XRD pattern with database files of the Joint Committee on Standards Powder Diffraction (JCPDS 16-427) shows the presence of $LiCoO_2$, the active cathode material most used by manufacturers of these types of batteries.

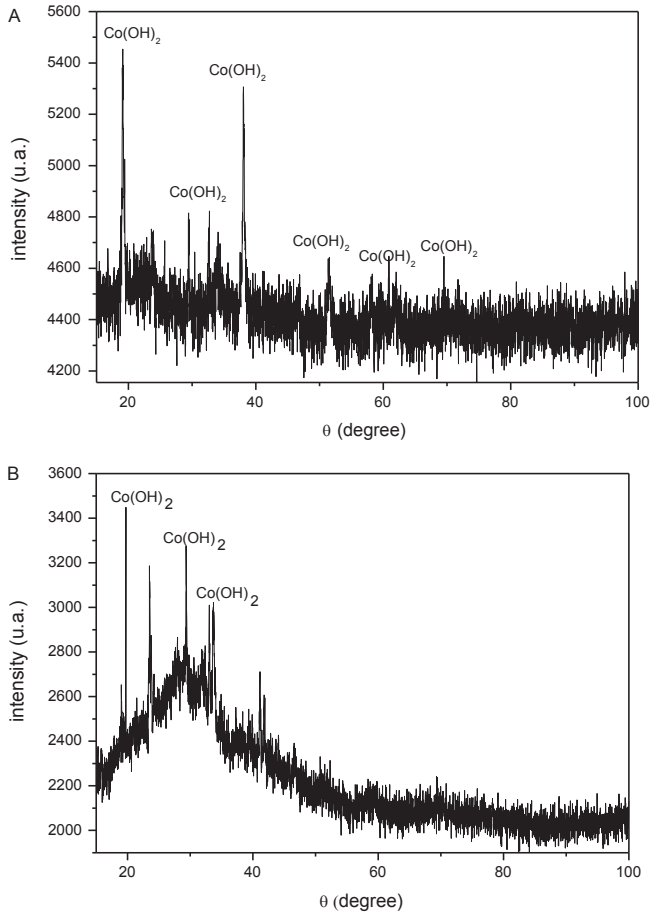

Fig. 4. X-ray diffraction spectrum of the $Co(OH)_2$ recovered by (A) chemical precipitation and (B) electrochemical precipitation (10 C cm^{-2}).

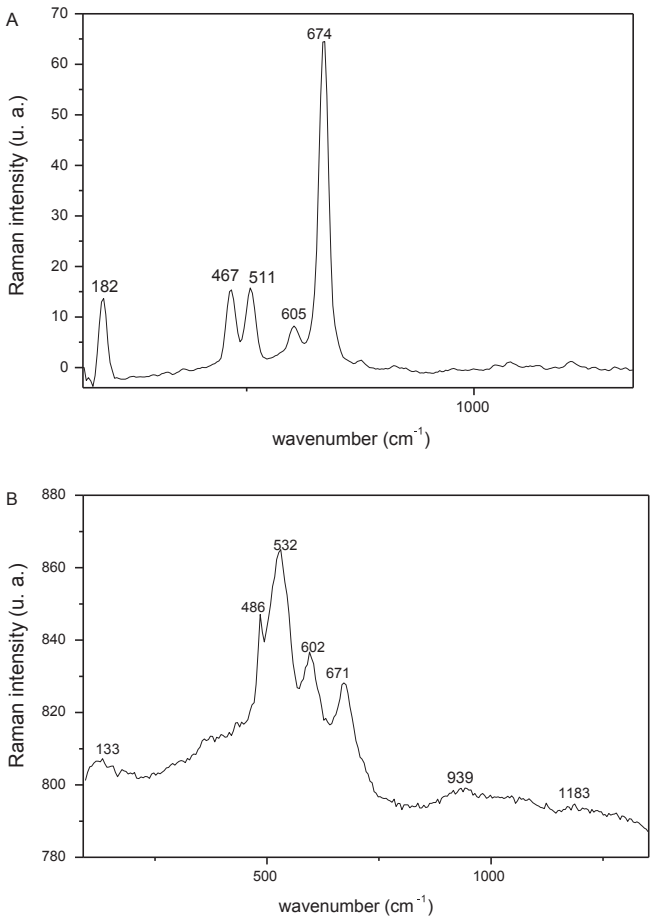

Fig. 5. Raman spectroscopy spectrum of the $Co(OH)_2$ recovered by (A) chemical precipitation and (B) electrochemical precipitation (10 C cm^{-2}).

3.2. Electrochemical formation of $Co(OH)_2$ films

CV was used to determine conditions for formation of $Co(OH)_2$ films (see Fig. 2). For all scan rates applied, formation of $Co(OH)_2$ on the electrode's surface was seen to take place in three

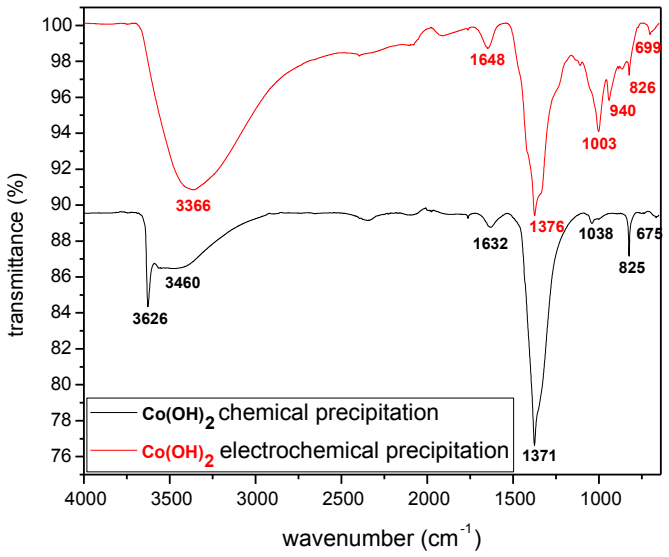

Fig. 6. Infrared spectroscopy spectrum of the $Co(OH)_2$ recovered by (A) chemical precipitation and (B) electrochemical precipitation(10 C cm^{-2}).

electrochemical and chemical stages. In Stage I, alkalinization of the electrode solution interface occurs, due to reduction reaction of nitrate ions and water containing dissolved oxygen. In Stage II, current density is independent of the potential. This type of behavior is associated with the process controlled by oxygen diffusion from the bulk solution to the electrode/solution interface. In Stage III, current density reaches a maximum value and then decreases due to the formation of $Co(OH)_2$ films on the electrode surface. At scan rates of 5.0 mV s^{-1} and 10.0 mV^{-1}, $Co(OH)_2$ films block passage of the current. From there to a scan rate of 1.0 mV^{-1}, current increases after the peak value is reached due to partial detachment of $Co(OH)_2$ films from the electrode. Potential for Stages I, II, and III to occur depends on the scan rate. The EP process for $Co(OH)_2$ films is described in Equations (3)–(5) [21–25].

Stage I: Alkalinization of electrode/solution interface.

$$NO_3^- + 7H_2O + 8e^- \rightarrow NH_4^+ + 10OH^- \quad (3)$$

Stage II: Process controlled by oxygen diffusion.

$$2H_2O + O_2 + 4e^- \rightarrow 4OH^- \quad (4)$$

Stage III: Formation of $Co(OH)_2$ films on the electrode surface.

$$Co^{2+} + 2OH^- \rightarrow Co(OH)_2 \quad (5)$$

Micrographs of $Co(OH)_2$ films were made by increasing the charge density, which further increases intensity of the reduction reaction of nitrate ions and water and, consequently, alkalinity at the electrode/solution interface. Fig. 3 shows the morphologies of the $Co(OH)_2$ films obtained, along with their various charge densities. In general, the micrographs from A to J form a compact, gray

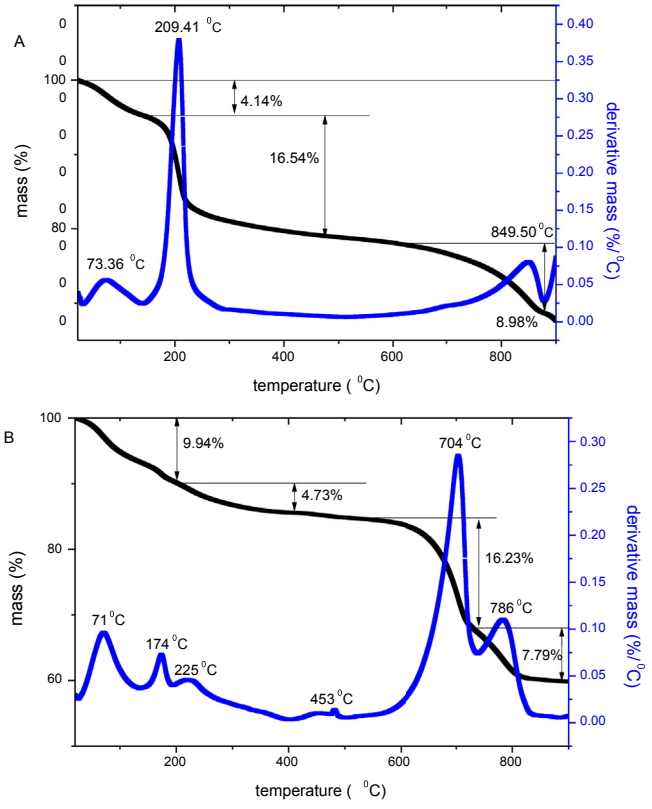

Fig. 7. Thermogravimetric curve for $Co(OH)_2$ recovered by (A) chemical precipitation and (B) electrochemical precipitation (10 C cm^{-2}) with an air atmosphere, scan rate of 10 °C min^{-1}, and alumina crucible.

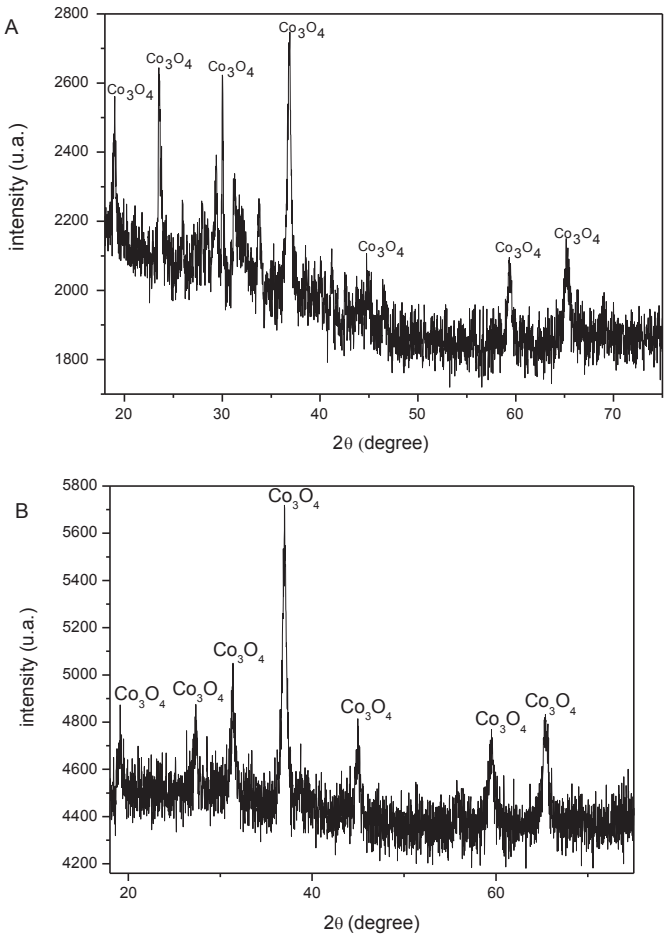

Fig. 8. X-ray diffraction spectrum of the Co_3O_4 synthesized from $Co(OH)_2$ obtained by (A) chemical precipitation and (B) electrochemical precipitation.

layer, which has cracks. As the charge density increases, the cracks decrease in length and quantity. A porous, white film grows on the compact layer. As charge density increases, the surface coverage of this porous film on the electrode increases. The surface films do not present a defined geometric form. The color contrast observed in the micrographs is an indication that compositions of the $Co(OH)_2$ films vary. Section 3.3 discusses characterization of the structure and composition of $Co(OH)_2$ films.

3.3. *Characterization of $Co(OH)_2$ obtained via chemical precipitation or electrochemical precipitation*

Fig. 4 shows that characterizations of $Co(OH)_2$ were obtained via x-ray diffraction using CP or EP (10 C cm^{-2}). Diffractogram peaks in Fig. 4A are in agreement with β-$Co(OH)_2$ (JCPDS 30-443), having a hexagonal structure. As shown in Fig. 4B, $Co(OH)_2$ obtained via EP appeared to be amorphous. This is in agreement with micrographs in Fig. 3.

Fig. 5 shows the Raman scattering spectra for $Co(OH)_2$, obtained via CP or EP. Peaks can be seen at 511 cm^{-1}, 605 cm^{-1}, and 674 cm^{-1} (CP) and at 532 cm^{-1}, 602 cm^{-1}, and 671 cm^{-1} (EP). These peaks are a result of stretching the Co–O binding. The peaks at 467 cm^{-1} (spectrum A, CP) and 486 cm^{-1} (spectrum B, EP) can be attributed to bending the O–Co–O [23].

Fig. 6 shows the infrared absorption spectra for the $Co(OH)_2$ obtained via CP or EP. In this figure, the absorption bands seen at 3626 cm^{-1} (CP) are due to the OH stretching of cobalt hydroxide,

and the bands at 3460 cm^{-1} (CP) and at 3366 cm^{-1} (EP) are due to the stretching vibration of the OH bond in H_2O molecules. The bands are wider for $Co(OH)_2$ obtained via EP because of its amorphous character. Angular stretches of water are found at 1632 cm^{-1} (CP) and at 1648 cm^{-1} (EP). The peaks at 1371 cm^{-1}, 1038 cm^{-1}, and 825 cm^{-1} (CP) and at 1376 cm^{-1}, 1003 cm^{-1}, and 826 cm^{-1} (EP) are associated with nitrate ions. The peaks at 699 cm^{-1} and 675 cm^{-1} are attributed to vibration in the plane of the ONO_2 [26].

Fig. 7A shows thermogravimetric analyses for the $Co(OH)_2$ obtained via CP, and Fig. 7B shows the $Co(OH)_2$ obtained via EP. For the $Co(OH)_2$ obtained via CP (Fig. 7A), mass loss is 4.14% w/w until a temperature of 150 °C was reached; this can be attributed to water desorption. The mass loss in the range of 150 °C–500 °C is a result of desorption of impurities, such as nitrate ions, and the dehydroxylation reaction of $Co(OH)_2$. The dehydroxylation of $Co(OH)_2$ corresponds to a theoretical mass loss of 13.62% w/w. In addition, the experiment determined a mass loss of 16.54% w/w due to presence of impurities in chemically precipitated $Co(OH)_2$. The mass loss that occurs in the range of 500 °C–900 °C, with a peak at 849 °C, can be attributed to the oxygen outlet from Co_3O_4 to CoO formation. The experimentally determined mass losses were 8.98% w/w and can be compared with the theoretical mass loss of 6.64% w/w [25,27].

For the $Co(OH)_2$ obtained using EP (Fig. 7B), the mass loss of 9.94% w/w, which occurred until a temperature of 200 °C was reached, can be attributed to water desorption. The higher mass loss for the $Co(OH)_2$ obtained via EP, which occurred until a temperature of 200 °C was reached, was due to its amorphous structure; this was also detected via x-ray diffraction (Fig. 3) and FT-IR (Fig. 5). The mass loss that occurred at 200 °C–500 °C was caused by desorption of impurities, such as nitrate ions detected in FT-IR measurements. The mass loss occurring in the 500 °C–900 °C temperature range, with peaks centered at 704 °C and 786 °C, can be attributed to $Co(OH)_2$ dehydroxylation reaction and output of oxygen from Co_3O_4 to formation of CoO. Equations (6) and (7) represent formation of Co_3O_4 and CoO from $Co(OH)_2$ obtained via CP or EP, respectively.

$$6Co(OH)_2 + O_2 \rightarrow 2Co_3O_4 + 6H_2O \quad (6)$$

$$2Co_3O_4 \rightarrow 6CoO + O_2 \quad (7)$$

Based upon characterization of $Co(OH)_2$ obtained via CP or EP, conditions for synthesis of the active material, Co_3O_4, were determined. The material precursor, $Co(OH)_2$, was heat-treated at 450 °C for 3 h in an air atmosphere. Peaks in the diffractograms shown in Fig. 8A and B are related to Co_3O_4 (JCPDS 43-1003): Both are cubic structures, indicating that the method of synthesis of the starting material, $Co(OH)_2$, had no influence on the structure of Co_3O_4. Fig. 9 shows the micrographs of the composite electrodes prepared with Co_3O_4. All micrographs reveal macropores of10 μm in length where the electrolyte diffuses from the bulk solution into the electrode surface. One also can visualize agglomerated crystals with an average length of 10 μm where the charge transfer reactions occur. Macroporosity is greater in the Co_3O_4 composite electrode formed from $Co(OH)_2$ via CP (Fig. 9A).

3.4. Electrochemical characterization of the Co_3O_4 composite electrodes

The CV shown in Fig. 10 was used for the electrochemical characterization of the Co_3O_4 composite electrodes. In the cathodic process, the CoO_2 undergoes a reduction to CoOOH, which then undergoes a further reduction to Co_3O_4. In this case, the CV has a shoulder at 0.430 V–0.450 V and a peak at 0.360–0.370 V (Equations (8) and (9)). The voltammograms (Fig. 10) show an anodic peak at 0.490 V–0.510 V, and in the cathodic process, there is a shoulder at 0.430 V–0.450 V and a peak at 0.360–0.370 V. In the anodic process, the Co_3O_4 undergoes oxidation to CoOOH, an intermediate species. In addition, CoOOH simultaneously undergoes further oxidation to CoO_2. In this case, there is only one anodic peak in the CV (Equation (10)). Oxidation and reduction reactions occurring with Co_3O_4 are represented by Equations (8)–(10) [28–30].

$$Co_3O_4 + OH^- + H_2O \rightleftarrows 3CoOOH + e^- \quad (8)$$

$$CoOOH + OH^- \rightleftarrows CoO_2 + H_2O + e^- \quad (9)$$

Total reaction.

$$Co_3O_4 + 4OH^- \rightleftarrows 3CoO_2 + 2H_2O + 4e^- \quad (10)$$

The Co_3O_4 composite electrode has good reversibility and charge efficiency (α), which is given by the following.

$$\alpha = q_{cathodic}/q_{anodic} \quad (11)$$

Fig. 11 shows charge efficiency for Co_3O_4 composite electrodes as a function of number of cycles. A maximum charge efficiency of 70% is obtained because oxygen evolution reaction occurs simultaneously with oxidation of Co_3O_4.

Fig. 11 shows that the charge efficiency depends on the scan rate. The charge transfer reactions occurring in electroactive areas

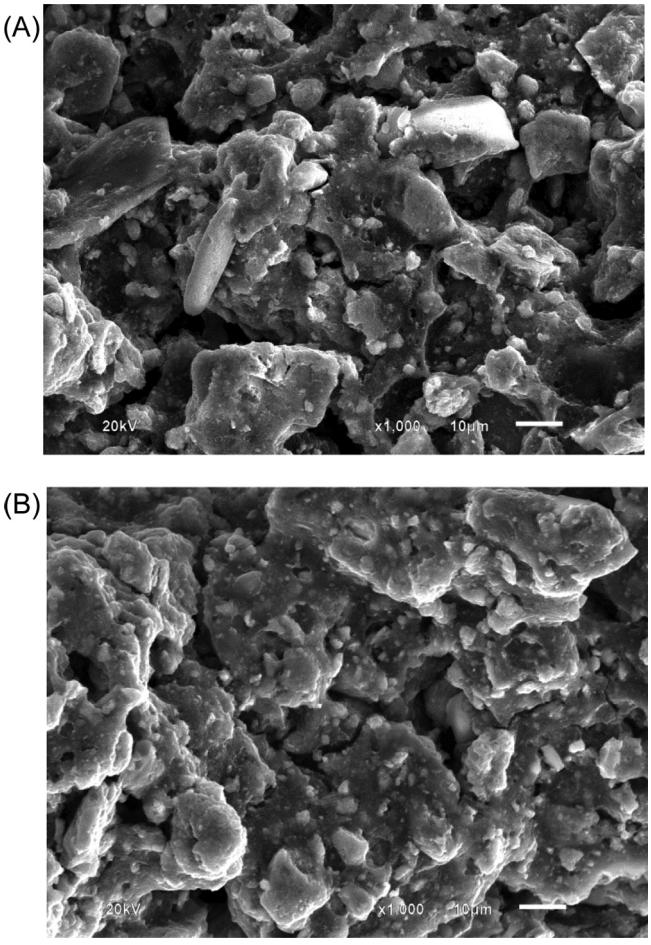

Fig. 9. Micrographs of the Co_3O_4 composite electrodes: (A) $CP80_{CB}$ and (B) $EP80_{CB}$.

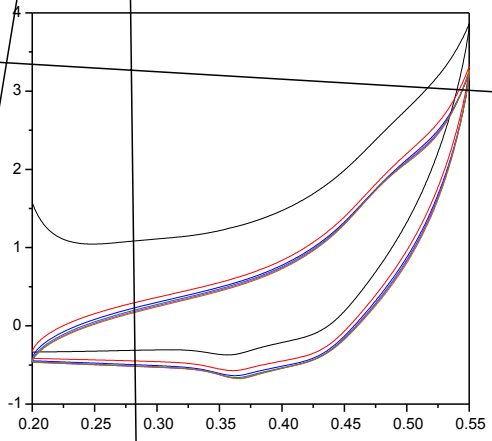

of the electrodes depend on the diffusion rate of the electrolyte from the solution volume phase to and inside of the agglomerated crystals. For slower scan rates, the diffusion time of the electrolyte to the electroactive area of the electrode is greater. Therefore, charge efficiency is greater for slower scan rates, and macroporosity has no influence.

The synthesis method of $Co(OH)_2$ has a low level of influence on the charge efficiency of Co_3O_4 at a scan rate of 1.0 mV s^{-1}. The charge efficiency at a scan rate of 10.0 mV s^{-1} is greater for $CP80_{CB}$ due to its greater macroporosity. The specific capacitance (C_m) of Co_3O_4 composite electrodes is given by the following equation.

$$C_m = Q/m\Delta V \tag{12}$$

where Q is the cathodic charge obtained with the GPES software, m is the mass of Co_3O_4, and ΔV is the variation of final and initial potential scans.

The specific capacitance at a scan rate of 1.0 mV s^{-1} for Co_3O_4 synthesized via heat treatment of $Co(OH)_2$ obtained by chemical or electrochemical precipitation is equal to 13.0 F g^{-1}. Co_3O_4 composite electrodes exhibit favorable characteristics for use as pseudocapacitors. The theoretical specific capacitance of Co_3O_4 is extremely high (3560 F g^{-1}) [31,32]. However, the specific capacitance observed for Co_3O_4 is much lower, and there still is the challenge of improving it. Further attempts to increase specific capacitance have been made via synthesis of nanostructured Co_3O_4 and use of carbon nanotubes in composite electrodes.

4. Conclusions

In this study, $Co(OH)_2$ was obtained using two methods: chemical precipitation (CP) and electrochemical (EP) (1.0 V vs. Ag/

AgCl). The charge density applied during electrodeposition of $Co(OH)_2$ directly affects its morphology: As the charge density increases, the $Co(OH)_2$ films, initially compact and cracked, are covered by a very porous film. Conditions for synthesis of the active material, Co_3O_4, were determined based on the characterization of the $Co(OH)_2$. The material precursor, $Co(OH)_2$, was heat-treated at 450 °C for 3 h in an air atmosphere. Co_3O_4 showed a cubic structure and presents a reasonable purity grade, regardless of the route used for preparation via which it was obtained. Electrochemical behavior of the composite electrodes then was evaluated using CV. The anodic peaks (0.47–0.48 V vs. Hg/HgO) and cathodic peaks (0.36–037 V and a shoulder at 0.430 V–0.450 V vs. Hg/HgO) in 6.0 mol L^{-1} KOH indicate that conversion of Co_3O_4 to CoO_2 can occur, with intermediate CoOOH consumption. A maximum charge efficiency of 70% was obtained because the oxygen evolution reaction occurs simultaneously with oxidation of Co_3O_4. The charge efficiency at a scan rate of 10.0 mV s^{-1} is greater for $CP80_{CB}$ due to its greater macroporosity. A specific capacitance of 13.0 F g^{-1} (1.0 mV s^{-1}) was observed in the Co_3O_4 composite electrodes. Therefore, in addition to presenting an alternative use for exhausted batteries, Co_3O_4 composites exhibit favorable characteristics for use as pseudocapacitors and have promise for applications in electrochemical devices.

Acknowledgments

The authors acknowledge NCQP, UFES, CAPES, FAPES, Laboratory Cellular Ultrastructure (CCS/UFES), Prof. Dr. Alfredo Gonçalves Cunha LPT/UFES e Laboratory DR-X/IFES.

References

[1] R. Moshtev, B. Johnson, J. Power Sources 91 (2000) 86–91.
[2] E.M. Garcia, J.S. Santos, E.C. Pereira, M.B.J.G. Freitas, J. Power Sources 185 (2008) 549–553.
[3] J.B. Goodenough, K.S. Park, J. Am. Chem. Soc. 135 (2013) 1167–1176.
[4] M.R. Awuala, M. Ismael, T. Yaitaa, Sens. Actuators B 191 (2014) 9–18.
[5] London Metal Exchange, www.lme.com, (accessed 02.03.14).
[6] H.S. Shim, V.R. Shinde, H.J. Kim, Y.-E. Sung, W.B. Kim, Thin Solid Films 516 (2008) 8573–8578.
[7] S. Vijayanand, R. Kannan, H.S. Potdar, V.K. Pillai, P.A. Joy, J. Appl. Electrochem. 43 (2013) 995–1003.
[8] Y.M. Kang, K.T. Kim, J.H. Kim, H.S. Kim, P.S. Lee, J.Y. Lee, H.K. Liu, S.X. Dou, J. Power Sources 133 (2004) 252–259.
[9] A. Pan, Y. Wang, W. Xu, Z. Nie, S. Liang, Z. Nie, C. Wang, G. Cao, J.G. Zhang, J. Power Sources 255 (2014) 125–129.
[10] T. Zhu, J.S. Chen, X.W. Lou, J. Mater. Chem. 20 (2010) 7015–7020.
[11] J. Jiang, W. Shi, S. Song, Q. Hao, W. Fan, X. Xia, X. Zhang, Q. Wang, C. Li, D. Yan, J. Power Sources 248 (2014) 1281–1289.
[12] C.W. Kung, H.W. Chen, C.-Y. Lin, R. Vittal, K.C. Ho, J. Power Sources 214 (2012) 91–99.
[13] D.D. Zhao, W.J. Zhou, H.L. Li, Chem. Mater. 19 (2007) 3882–3891.
[14] R. Hallaj, K. Akhtari, A. Salimi, S. Soltanianc, Appl. Surf. Sci. 276 (2013) 512–520.
[15] A. Burke, J. Power Sources 91 (2000) 37–50.
[16] X.H. Xia, J.P. Tu, J. Zhang, J.Y. Xiang, X.L. Wang, X.B. Zhao, Sol. Energy Mater. Sol. Cells 94 (2010) 386–389.
[17] J.-C. Chen, C.-T. Hsu, C.-C. Hu, J. Power Sources 253 (2014) 205–213.
[18] L.B. Kong, J.W. Langa, M. Liu, Y.C. Luo, L. Kang, J. Power Sources 194 (2009) 1194–1201.
[19] M. Contestabile, S. Panero, B. Scrosati, J. Power Sources 83 (1999) 75–78.
[20] L. Xie, K. Li, G. Sun, Z. Hu, C. Lv, J. Wang, C. Zhang, J. Solid State Electrochem. 17 (2013) 55–61.
[21] X. Sun, X.Q. Yang, J. McBreen, Y. Gao, M.V. Yakovleva, X.K. Xing, M.L. Daroux, J. Power Sources 97–98 (2001) 274–276.
[22] W.J. Zhou, D.D. Zhao, M.W. Xu, C.L. Xu, H.L. Li, Electrochim. Acta 53 (2008) 7210–7219.
[23] X.F. Wang, Z. You, D.B. Ruan, Chin. J. Chem. 24 (2006) 1126–1132.
[24] J.R.S. Brownson, C. Lévy-Clément, Electrochim. Acta 54 (2009) 6637–6644.
[25] J. Yang, H. Liu, W.N. Martens, R.L. Frost, J. Phys. Chem. C 114 (2010) 111–119.
[26] R. Xu, H.C. Zeng, Chem. Mater. 15 (2003) 2040–2048.
[27] C.W. Tang, C.-B. Wang, S.H. Chien, Thermochim. Acta 473 (2008) 68–73.
[28] Y.Y. Gao, S.L. Chen, D.X. Cao, G.L. Wang, J.L. Yin, J. Power Sources 195 (2010) 1757–1760.
[29] X.H. Xia, J.P. Tu, Y.J. Mai, X.L. Wang, C.D. Gu, X.B. Zhao, J. Mater. Chem. 21 (2011) 9319–9325.
[30] G.I. Casella, M. Gatta, J. Electroanal. Chem. 534 (2002) 3–38.
[31] H. Cheng, Z.G. Lu, J.Q. Deng, C.Y. Chung, K. Zhang, Y.Y. Li, Nano Res. 3 (2010) 895–901.
[32] T.-Y. Wei, C.-H. Chen, K.-H. Chang, S.-Y. Lu, C.-C. Hu, Chem. Mater. 21 (2009) 3228–3233.